

Core to ultracompact H_{II} region evolution in the W49A massive protocluster

T. Nony^{1,2}, R. Galván-Madrid², N. Brouillet³, G. Suárez⁴, F. Louvet⁵, C. G. De Pree⁶, M. Juárez-Gama⁷, A. Ginsburg⁸, K. Immer⁹, Y. Lin¹⁰, H. B. Liu^{11,12}, C. G. Román-Zúñiga¹³, and Q. Zhang¹⁴

¹ INAF - Osservatorio Astrofisico di Arcetri, Largo E. Fermi 5, 50125 Firenze, Italy e-mail: thomas.nony@inaf.it

² Instituto de Radioastronomía y Astrofísica, Universidad Nacional Autónoma de México, Morelia, Michoacán 58089, Mexico

³ Laboratoire d'astrophysique de Bordeaux, Univ. Bordeaux, CNRS, B18N, allée Geoffroy Saint-Hilaire, 33615 Pessac, France

⁴ Department of Astrophysics, American Museum of Natural History, Central Park West at 79th Street, NY 10024, USA

⁵ Univ. Grenoble Alpes, CNRS, IPAG, 38000 Grenoble, France

⁶ National Radio Astronomy Observatory, 520 Edgemont Road, Charlottesville, VA 22903

⁷ Instituto Nacional de Astrofísica, Óptica y Electrónica, Luis E. Erro 1, 72840 Tonantzintla, Puebla, Mexico

⁸ Department of Astronomy, University of Florida, PO Box 112055, USA

⁹ Leiden Observatory, Leiden University, PO Box 9513, 2300 RA Leiden, The Netherlands

¹⁰ Max-Planck-Institut für Extraterrestrische Physik, Giessenbachstr. 1, 85748 Garching bei München, Germany

¹¹ Department of Physics, National Sun Yat-Sen University, No. 70, Lien-Hai Road, Kaohsiung City 80424, Taiwan, R.O.C.

¹² Center of Astronomy and Gravitation, National Taiwan Normal University, Taipei 116, Taiwan

¹³ Universidad Nacional Autónoma de México, Instituto de Astronomía, AP 106, Ensenada 22800, BC, Mexico

¹⁴ Center for Astrophysics, Harvard & Smithsonian, 60 Garden St., Cambridge, MA 02420, USA

April 4, 2024

ABSTRACT

Aims. We aim to identify and characterize cores in the high-mass proto-cluster W49, determine their evolutionary stages and measure the associated lifetimes.

Methods. We built a catalog of 129 cores extracted from an ALMA 1.3 mm continuum image at 0.26'' (2900 au) angular resolution. The association between cores and Hyper/Ultra Compact H_{II} (H/UC H_{II}) regions was established from the analysis of VLA 3.3 cm continuum and H30 α line observations. We also looked for emission of hot molecular cores (HMCs) using the methyl formate doublet at 218.29 GHz.

Results. We identified 40 cores associated with an H/UC H_{II} region and 19 HMCs over the ALMA mosaic. The 52 cores with an H/UC H_{II} region and/or a HMC are assumed to be high-mass protostellar cores, while the rest of the core population likely consists in prestellar cores and low-mass protostellar cores. We found a good agreement between the two tracers of ionized gas, with 23 common detections and only four cores detected at 3.3 cm and not in H30 α . The spectral indexes from 3.3 cm to 1.3 mm range from 1, for the youngest cores with partially optically thick free-free emission, to about -0.1, that is optically thin free-free emission obtained for cores likely more evolved.

Conclusions. Using as a reference the H/UC H_{II} regions, we found the statistical lifetimes of the HMC and massive protostellar phases in W49N to be about 6×10^4 yr and 1.4×10^5 yr, respectively. We also showed that HMC can co-exist with H/UC H_{II} regions during a short fraction of the core lifetime, about 2×10^4 yr. This indicates a rapid dispersal of the inner molecule envelope once the H/UC H_{II} is formed.

Key words. stars: formation – stars: protostars – stars: massive – ISM: clouds – ISM: HII regions

1. Introduction

The evolutionary sequence and timescales of the formation of high-mass stars are still poorly constrained (see e.g., the review by Motte et al. 2018), partly because of observational difficulties related to low-number statistics and large distances within the Milky Way. W49A is among the few molecular clouds that enable us to study, in a single region and with robust statistics, various evolutionary stages of high-mass star formation. Young, massive protostars first drive strong molecular outflows and heat the inner part of their envelope. Complex organic molecules (COMs) are released from the grains in the heated region (Herbst & van Dishoeck 2009), which is called hot molecular core (HMC) and is thus characterized by multiple lines from COMs - the so called "line forest". Contrarily to their low-mass analogs,

high-mass protostars are still embedded in their nascent envelope when they evolve to the main sequence. The extreme ultraviolet (EUV) radiation from high-mass stars ($>8 M_{\odot}$) is sufficient to ionize hydrogen and create an H_{II} region (Churchwell 2002). As the luminosity of the star keeps increasing, the H_{II} region expands and breaks through the core, and eventually impacts the whole molecular cloud. Hypercompact (HC) H_{II} regions are usually interpreted as the youngest stage of ionization by a massive star (e.g., Keto 2007; Tanaka et al. 2016), confined to within cores to sizes $\sim 10^{-2}$ pc, or even less, and having electron densities $n_e > 10^6$ cm $^{-3}$ (Kurtz 2005). Ultracompact (UC) H_{II} regions are, by definition, expected to be larger and less dense by at least one order of magnitude. However, deep centimeter surveys of protocluster regions (e.g., Ginsburg et al. 2016) have shown that the most common type of hypercompact sized H_{II} regions have

lower densities, in the range 10^4 to $< 10^6$ cm^{-3} (Rivera-Soto et al. 2020). Since a reliable distinction between these two types of objects requires modeling of the cm to (sub)mm spectral energy distribution (e.g., Keto et al. 2008; Galván-Madrid et al. 2009; Zhang et al. 2022), we refer to all our detections of small HII emission as H/UC HII regions.

W49A, located at a distance of 11.1 kpc from the Sun (Zhang et al. 2013), is one of the most luminous protoclusters in the Galaxy ($L \sim 2.6 \times 10^7 L_\odot$, Sievers et al. 1991; Lin et al. 2016). The W49A giant molecular cloud (GMC) has been mapped from ~ 100 pc to sub-pc scales in the (sub)millimeter continuum and in molecular lines, down to angular resolutions of a few arcseconds (e.g., Miyawaki et al. 2009; Peng et al. 2010; Galván-Madrid et al. 2013; Barnes et al. 2020). The W49A GMC can be divided in three subcomponents labeled W49 north (W49N), W49 south (W49S), and W49 south-west (W49SW). From CO observations, Galván-Madrid et al. (2013) evaluated the gas mass of the W49A GMC within a radius of 60 pc to be $10^6 M_\odot$, with the main star-forming hub W49N concentrating $M_{\text{gas}} \sim 2 \times 10^5 M_\odot$ within a radius of 6 pc. A cluster of massive stars with a total mass of about $10^4 M_\odot$ has been identified in the near infrared by Homeier & Alves (2005), at about 3 pc east of the center of W49N. The study of Saral et al. (2015) with *Spitzer* also revealed 232 Class 0/I Young Stellar Objects in the entire W49A GMC. About 50 HC and UC HII regions have been detected in W49A (e.g., Welch et al. 1987; De Pree et al. 1997, 2020). The embedded and infrared-visible stellar populations drive already significant feedback across the GMC (Rugel et al. 2019). Prominent water maser features extending to hundreds of kilometers per second from the cloud velocity have been reported within W49N (e.g., Gwinn et al. 1992; McGrath et al. 2004). Also, five 6.7 GHz methanol masers were reported the catalog of Breen et al. (2015). Finally, Wilner et al. (2001) reported the detection of 6 HMCs in W49N using CH_3CN observations at subarcsecond resolution, and Miyawaki et al. (2022b) studied the HMC W49N MCN-a (UCHII region J1 in De Pree et al. 1997).

The star forming core population and star formation sequence in W49A have however not been explored in detail so far. In this work, we present a subarcsecond resolution study of W49A aimed at identifying and characterizing its core populations, as well as the evolutionary sequence from young star forming cores to UCHII regions. The ALMA and VLA observations we used are presented in Section 2. The analysis of the continuum maps and molecular lines presented in Section 3 is used in Section 4 to characterize the dust cores and establish a temporal classification based on their association with hot molecular cores and UC HII regions. A discussion is proposed in Section 5 and Section 6 summarizes our main conclusion.

2. Observations

2.1. ALMA data

Observations of W49A at 1.3 mm (Band 6) were carried out with ALMA in Cycle 5 (project 2016.1.00620.S, PIs: Ginsburg, Galván-Madrid) between 2017 and 2018. The data consist in a mosaic of 28 fields with a primary beam of $25.6''$, for a total mapping extent of about $2.5' \times 1.6'$ (8.2×5.3 pc). The maximum recoverable scale of the 12-m array configuration used in this work is about $11''$.

Continuum data were processed with CASA version 5.4 (CASA Team et al. 2022) using the imaging and self-calibration pipeline developed by the ALMA-IMF consortium (described in

detail in Ginsburg et al. 2022). The continuum map has been produced using a selection of line-free channels (equivalent to the cleanest maps in Ginsburg et al. 2022) from the four spectral windows (hereafter Spws) of the dataset, summing up to a bandwidth of 1.23 GHz. We performed three iterations of cleaning and phase self-calibration and one iteration of amplitude self-calibration, using model masks of increasing size and decreasing cleaning thresholds. We used the Multi-term (Multi Scale) Multi-Frequency Synthesis deconvolver of *tclean* with two Taylor terms, a robust parameter of 0, and scales up to nine times larger than the synthesized beam. The final beam of the 1.3 mm continuum image has a FWHM size of $0.29'' \times 0.24''$ (≈ 2900 au at 11.1 kpc). The rms noise measured in regions far away from the brightest emission, where the map is not limited by dynamic range, is of 0.38 mJy beam $^{-1}$ (see Table 1).

For the line data, the four spectral windows were processed with IMAGER¹, implemented within the GILDAS software². Cleaning was performed using Clark deconvolution and 0.1 robust weighting. The cubes across the four bands have a spatial resolution of approximately $0.24''$ (2750 au), a channel width of 0.65 km s $^{-1}$, and an rms noise of 1.6 mJy beam $^{-1}$ (0.6 K) per channel. The detailed parameters for each spectral window are given in Table 1. We have used the method presented in Molet et al. (2019) and Brouillet et al. (2022) to separate the continuum and spectral line emission in each pixel of the image plane. The Spw 2 band covers the H30 α line at 231.9 GHz. We also used the Spw 0 and Spw 3 bands to analyze CH_3OCHO lines.

2.2. VLA data

We used the VLA A-array continuum image at 3.3 cm (X Band) presented in De Pree et al. (2020). This image was created with the purpose of only studying W49N. Its field of view is outlined in Fig. 1. We smoothed this image from its original angular resolution ($0.16''$) to the resolution of the B6 ALMA continuum image ($0.26''$), then corrected it for its primary-beam response and regridded it to the ALMA image frame.

Juárez-Gama et al. (in prep.) used this image to provide a dendrogram catalog of H/UC HII regions and their physical properties in W49N. Their catalog of 79 H/UC HII regions is consistent with, and more complete, than previous visual identifications of H/UC HII regions in this protocluster (e.g., De Pree et al. 2005, 2020). We used the cm continuum catalog of Juárez-Gama et al. to complement the identification of dust cores and HMCs reported in this paper, as well as the HII emission traced by H30 α also presented in this paper.

3. Analysis of the continuum maps and molecular lines

3.1. Core catalog

We used the *getsf* algorithm (Men'shchikov 2021) to extract sources from the 1.3 mm continuum images. *getsf* decomposes the image into various spatial scales and separates compact sources from their background and filamentary structures. It is therefore well suited to find cores in complex environments such as high-mass star-forming regions. *getsf* has been extensively used in ALMA studies of protocluster regions (e.g., Pouteau et al. 2022; Nony et al. 2023). We found 129 cores passing the post-selection filters for robust detection and measurements

¹ <https://imager.oas.u-bordeaux.fr>

² <http://www.iram.fr/IRAMFR/GILDAS>

Table 1. Parameters of the continuum images and spectral cubes.

Image	Instr.	$\nu_{\text{obs}}^{\text{a}}$	Bandwidth ^b	pixel	Resolution ^c		1σ rms
		[GHz]			[MHz]	['' \times '']	
X band cont.	VLA	9.107	688	0.06	0.29 \times 0.24	-	0.22
Band 6 cont.	ALMA	227.950	1230	0.06	0.29 \times 0.24	-	0.38
Spw 0	ALMA	217.900	1875	0.07	0.28 \times 0.23	0.67	1.47
Spw 1	ALMA	219.860	1875	0.07	0.28 \times 0.25	0.67	1.67
Spw 2/H30 α	ALMA	231.870	1875	0.07	0.27 \times 0.20	0.63	1.57
Spw 3	ALMA	233.740	1875	0.07	0.27 \times 0.20	0.63	1.57

^a Central frequency of the continuum images or of the spectral windows. The central frequency of the ALMA continuum image is computed as the intensity-weighted average frequency, with a spectral index of 3 (see Eq. 1 in Ginsburg et al. 2022).

^b Bandwidth used to create the continuum images or bandwidth of the cubes.

^c Beam FWHM and channel width. The data cubes have been produced using the default Hanning smoothing function without channel averaging ($N=1$), resulting in a spectral resolution of two channels.

^d 1 mJy beam⁻¹ corresponds to 0.34 K at 230 GHz and to 222 K at 9 GHz for the continuum maps.

recommended by Men'shchikov (2021): signal-to-noise for the background-subtracted peak larger than two, source size smaller than four times the FWHM beamsize, and ellipticity smaller than two. Table A1 lists the retrieved parameters of the identified cores: position, major and minor axis FWHM, and position angle.

We also used *getsf* to measure the peak intensity and integrated flux of the cores in the ALMA B6 ($S_{\text{B6}}^{\text{peak}}$, $S_{\text{B6}}^{\text{int}}$) and VLA X-band ($S_{\text{BX}}^{\text{peak}}$, $S_{\text{BX}}^{\text{int}}$) maps. Cores are marked in the B6 continuum map in Fig. 1 and in zoom-in Figs. 2 and 3. Complementary, we measured directly in the continuum maps the maximum intensity of cores in both B6 and X band, F^{max} , and computed the integrated flux from the sum of the pixel intensities (I) within the core FWHM: $F^{\text{int}} = c \sum I A_{\text{pix}} / A_{\text{beam}}$; with A_{pix} the pixel area and $A_{\text{beam}} = \pi \theta_{\text{min}} \theta_{\text{maj}} / (4 \ln(2))$ the beam area. We set the constant $c=1/\ln(2)$ to account for the core extension beyond its FWHM. We used this second set of parameters for the calculations presented in Section 4.2, in which we compare a continuum map dominated by thermal dust emission (ALMA B6 at 230 GHz) with one dominated by free-free emission (VLA X-band at 9 GHz).

3.2. Recombination line and free-free emission

We identified cores associated with H/UC HII regions using two tracers of ionized gas, the H30 α recombination line and the free-free emission measured using the X-band map.

3.2.1. Detection of the H30 α line

We identified cores associated with H30 α emission using two complementary methods. Our first method is as follows: for all the cores we inspected the spectrum at the frequency of the H30 α line and performed Gaussian fitting to measure the line systemic velocity, the FWHM line width ΔV , and the peak brightness temperature T_{B} . We then separated cores with brightness temperature $T_{\text{B}} > 2$ K (38 cores) from cores with T_{B} between 0.8 and 2 K (14 cores). There are ³³SO₂ (12_{3,9} – 12_{2,10}) lines very close in frequency (231.9004 GHz, 231.9015 GHz) to the H30 α line at

³ Contrarily to the peak intensity in X band $S_{\text{BX}}^{\text{peak}}$, which is measured at the center of the ellipse defined in the B6 map, $F_{\text{BX}}^{\text{max}}$ is measured on the brightest pixel within the ellipse.

231.9009 GHz, as well as CH₃C¹⁵N and CH₃OCHO lines within 3 MHz. Therefore, disentangling the H30 α emission can be challenging. Since the H30 α line is expected to be much broader (see, e.g., the review of Hoare et al. 2007), we further applied a threshold for the linewidth of $\Delta V > 20$ km s⁻¹ to filter out cores dominated by contamination from molecular lines. This gave us 29 remaining cores with strong H30 α detection ($T_{\text{B}} > 2$ K) and 9 with a weak detection.

Our second method relies on moment 0 maps of the H30 α line, which we constructed by integrating in velocity from -50 km s⁻¹ to $+50$ km s⁻¹ (the line systemic velocity ranges from about 0 to 20 km s⁻¹ LSR). We considered a positive detection when the core's FWHM ellipse includes a group of pixels above a given threshold. Considering the large dynamic range of the line emission in the map, we noticed that the noise strongly decreases from the center to the edges of the mosaic. In consequence, we defined two reference thresholds, $5\sigma_{\text{ctr}} = 0.4$ Jy beam⁻¹ km s⁻¹ in the center, $5\sigma_{\text{sw}} = 0.1$ Jy beam⁻¹ km s⁻¹ in the South West (SW) region, and we constructed a clipped moment 0 map where pixels below 5σ are set to zeros. All the 29 cores with a strong H30 α line detection are also detected in the moment 0 maps and qualify as robust H30 α detections. On the other hand, the nine cores with weak H30 α line detection using the first method have a few isolated pixels above their respective threshold at most, and are considered as tentative H30 α detections. Cores with a robust or tentative H30 α detection are overlaid on the moment 0 maps in the bottom panels of Figs. 2 and 3.

3.2.2. Detection of free-free centimeter emission

We defined the criterion for a robust detection and measurement in X band as $S_{\text{BX}}^{\text{peak}} > 3\sigma_{\text{BX}}$ and $F_{\text{BX}}^{\text{max}} > 3\sigma_{\text{BX}}$, where $\sigma_{\text{BX}} = 0.22$ mJy beam⁻¹ is the noise in the X band maps convolved to the B6 angular resolution, measured using the median absolute deviation. This criterion combines the background subtracted peak intensity S^{peak} determined by *getsf* and the maximum intensity measured in the original continuum map (see Section 3.1). Out of the 109 cores lying in the field of view of the X band map, 27 have a robust detection at 3.3 cm. Table A1 lists the integrated core fluxes in X band ($F_{\text{BX}}^{\text{int}}$) and Band 6 ($F_{\text{B6}}^{\text{int}}$).

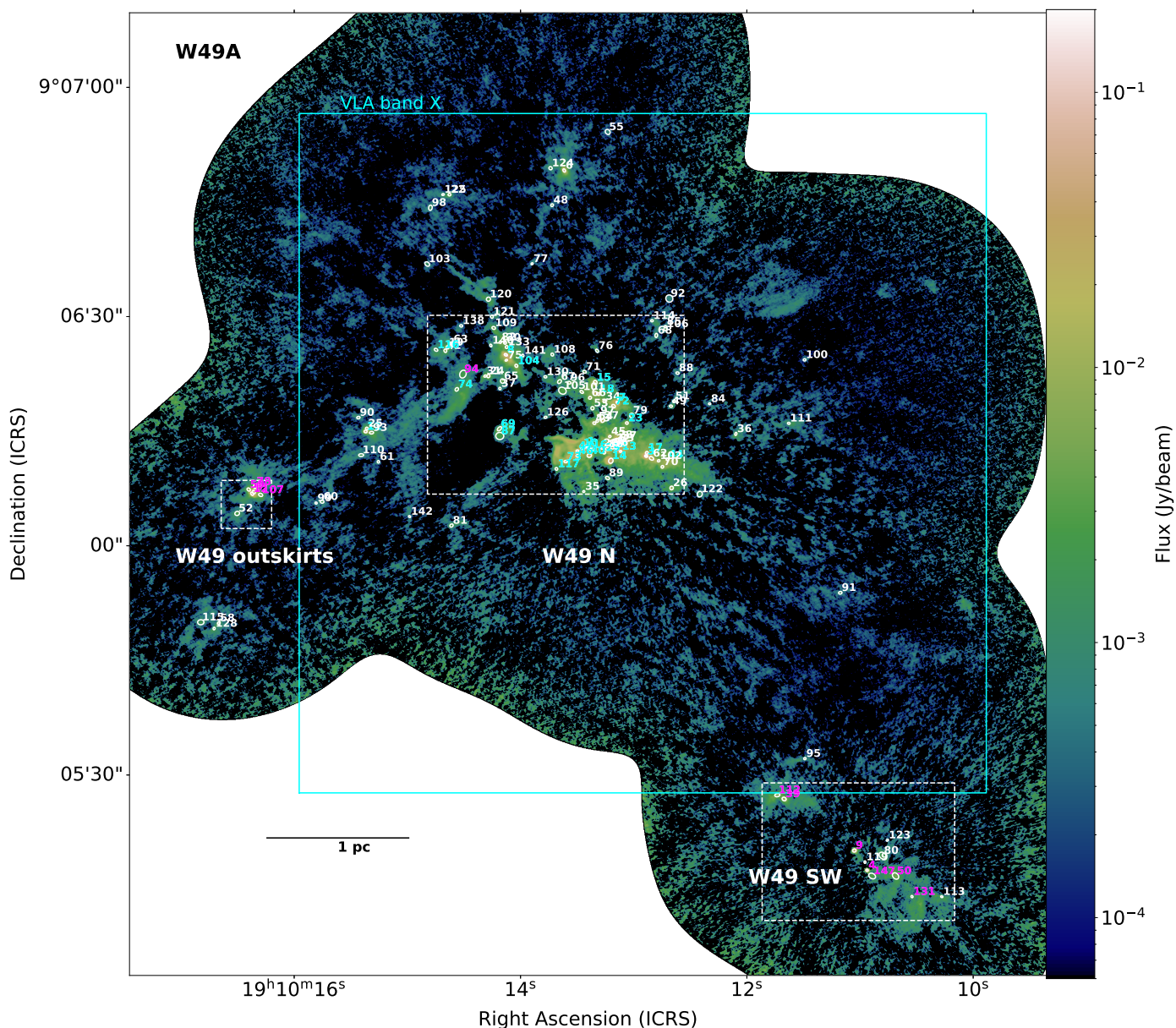


Fig. 1. The W49A protocluster region as imaged at 1.3 mm using ALMA. Dust cores are represented by their FWHM ellipses in white, and numbered in cyan for cores also detected at 3.3 cm, in magenta for cores detected only in H30 α , and white for non detections at 3.3 cm nor H30 α . The field of view of the VLA X band image is represented in solid cyan line. A scale bar is shown. Zoom-ins toward the three main regions of interest (W49N, W49SW and W49 outskirts), delimited by white dashed lines, are shown in Figs. 2 and 3.

3.3. Identification of hot molecular cores

We used methyl formate (CH₃OCHO) as a signature of hot molecular core emission, following the method described in Brouillet et al. (2022) where it was found that the use of methyl formate to identify the main HMCs in the W43-MM1 region provides similar results compared to the use of a broad frequency band with various other lines of complex organic molecules (see their Fig. 5). This study showed that this molecule offers a good compromise between widespread detectability and reliability in tracing HMC. Methyl formate has also been used to identify HMC candidates in the recent survey of Bonfand et al. (2024). We have based the identification on the CH₃OCHO (17_{3,14} – 16_{3,13}) doublet at 218.281 and 218.298 GHz, with an upper-level energy E_u of 99.7 K. We have further verified our detections with a synthetic spectrum fitting the numerous methyl formate lines

in Spw 3. We found 19 dust cores with HMC emission within the entire ALMA mosaic, that is 17 within the field of view of the X band map and 2 in the south-western region. They are indicated with an asterisk in Table A1.

4. Characterization of dust cores

From the measurements presented in Section 3, we identify cores associated with H/UC HII regions in Section 4.1 and measure their properties in Section 4.2. The inclusion of HMCs enables us to refine the evolutionary status of cores in Section 4.3.

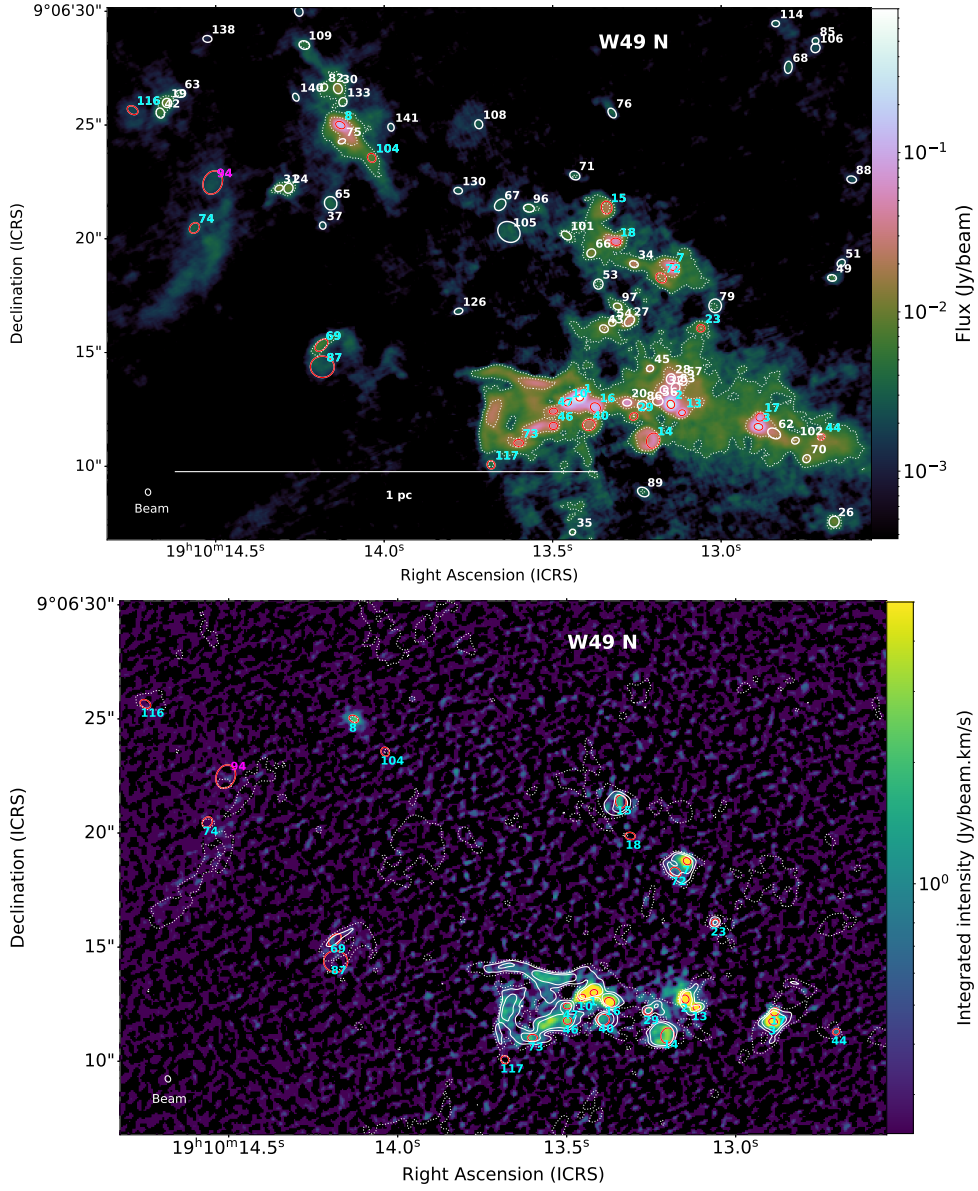


Fig. 2. 1.3 millimeter continuum and recombination line maps toward W49N at the center of W49A. Top panel: ALMA B6 continuum image, contours are 10 and 40 sigma. Bottom panel: moment 0 map of H30 α (color) and VLA X-band map (contours). Contours are 3 sigma (dotted lines), 15, and 40 sigma (solid lines). Dust cores are represented by their FWHM ellipses and numbered with the same colors as in Fig. 1. Cores detected in X band and/or in H30 α are shown in red, the top panel also shows the remainder of the core catalog in white. Beams are shown in the lower left corner. A scale bar is shown in the top panel.

4.1. Classification of cores with H/UCHII regions

4.1.1. With VLA measurements

For 109 cores within the field of view of the X band image, we have information on both the X band and the H30 α detection. The 27 cores with a robust detection in X band are likely associated with an H/UCHII region. 20 are also detected in H30 α and three have a tentative H30 α detection (#74, #87, #116). The remaining four cores without detection in H30 α (#8, #18, #104, #117) only have a weak X band detection, with $S_{\text{BX}}^{\text{peak}}$ and $F_{\text{BX}}^{\text{max}}$ between 3 and $10\sigma_{\text{BX}}$, which suggests that our sensitivity to detect ionized gas is higher in the X band map than with the recombination line. Two other cores have a tentative H30 α detection and no detection in X band: after visual inspection core #94 is considered as an H/UCHII region candidate and core #82 is rejected.

Our identification of dust cores associated with H/UCHII regions largely overlaps with the independent dendrogram catalog of H/UCHII regions of Juárez-Gama et al. (in prep.) (see Section 2.2). 21 H/UCHII dendrogram structures out of 79 within the X band map are associated with a core with H/UCHII region, as previously defined. In detail, 20 HII dendrogram structures are associated with 26 cores with a robust detection in X band⁴ Only one HII dendrogram structure is associated with a dust core (#27) not detected in X band. Conversely, only one dust core with a detection in X band is not associated with a dendrogram structure. This core (#18) is among the weakest X band detections ($S_{\text{BX}}^{\text{peak}} = 4\sigma_{\text{BX}}$ and $F_{\text{BX}}^{\text{max}} = 3.4\sigma_{\text{BX}}$) and is not found in H30 α . Fifty seven structures in the dendrogram catalog built

⁴ 5 dendrogram HII structures are associated with more than one dust core.

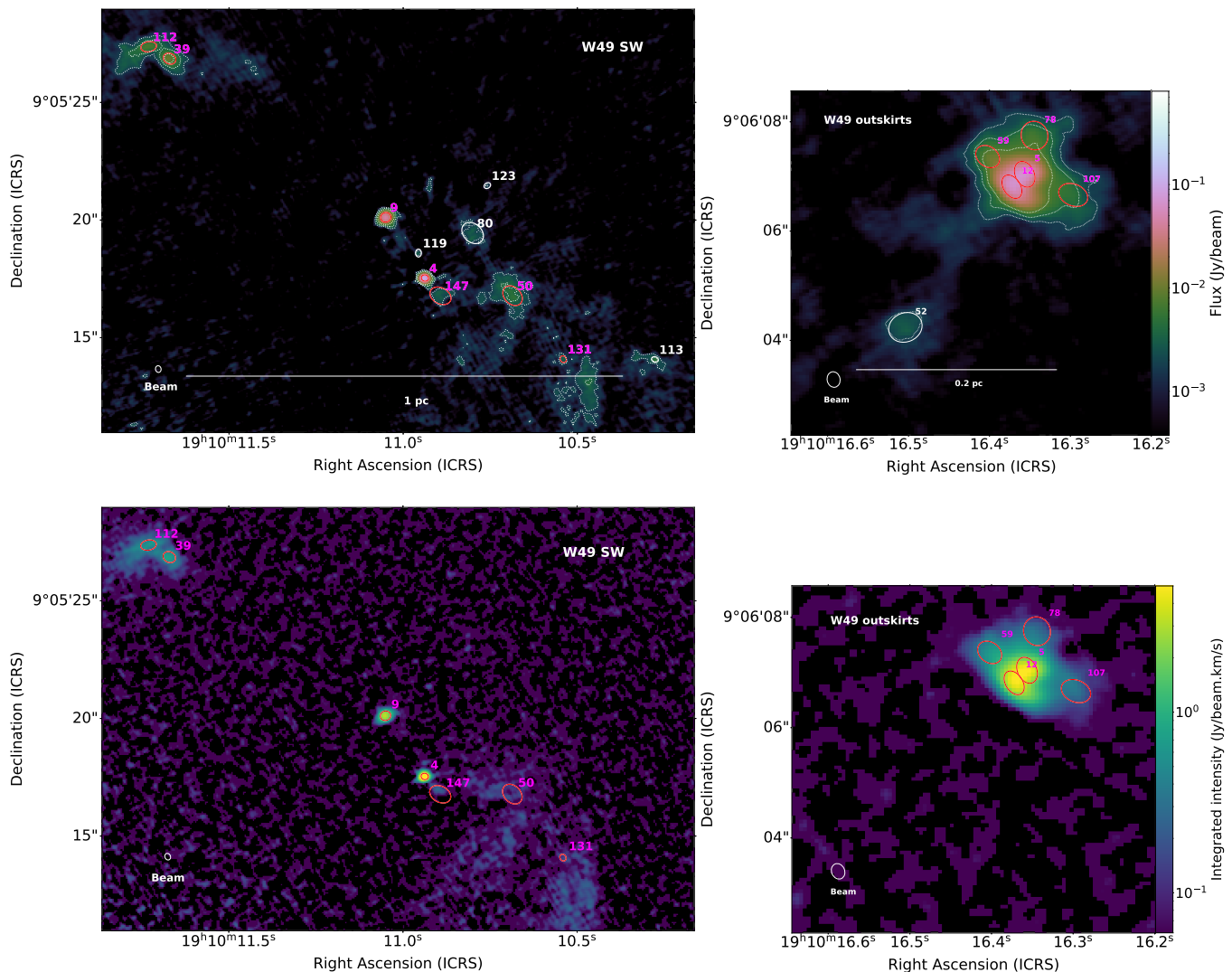


Fig. 3. 1.3 millimeter continuum and recombination line maps toward W49 SW (left panels) and the eastern outskirts (right panels). Top panel: B6 continuum image. Contours are 5, 10, and 20 sigma. Bottom panel: moment 0 map of H30 α line. The same conventions of Fig. 2 apply for ellipses and lines.

from the X band map do not have any counterpart in the Band 6 core catalog and qualify as H/UC HII regions without association to dust cores. A summary of the relation between the 28 dust cores associated with H/UC HII regions (27 when excluding the H/UC HII region candidate) and the dendrogram-identified H/UC HII regions is shown in Fig. 4.

4.1.2. Without VLA measurements

For the 20 dust cores outside the field of view of the X band image, the recombination line is the only tool to search for emission from H/UC HII regions. Nine cores associated with a robust H30 α detection (four in the southwestern region, five in the eastern outskirts, see Fig. 4) are likely associated with an H/UC HII region. After visual inspection, three additional cores with a tentative H30 α detection located in the SW region (#50, #131, #147) are considered as H/UC HII region candidates, and another core located in the eastern outskirts (#115) is rejected.

4.2. Free-free emission in ALMA Band 6

Out of the 129 dust cores detected with ALMA over the entire mosaic, we found 36 cores associated with H/UC HII regions (27 with VLA measurements, 32 with H30 α measurements, see Section 4.1) and 4 cores tentatively associated with H/UC HII regions (#50, #94, #131, #147), which have only tentative H30 α detections.

A first evaluation of their free-free emission at 1.3 mm is obtained from the integrated fluxes, $F_{\text{BX}}^{\text{int}}$ measured in the X band map over FWHM of the cores (see Section 3.1):

$$F_{\text{ff,cm}}^{\text{int}} = F_{\text{BX}}^{\text{int}} \left(\frac{\nu_{\text{B6}}}{\nu_{\text{BX}}} \right)^{\alpha}, \quad (1)$$

where $\nu_{\text{B6}} = 227.95$ GHz and $\nu_{\text{BX}} = 9.11$ GHz are the reference frequency of the ALMA B6 and VLA X band images, respectively (see Table 1). We took a spectral index $\alpha = -0.1$, assuming that the free-free emission is optically thin all the way from 3 cm to 1 mm. The fluxes calculated in this way are thus lower limits to the free-free emission in the ALMA image.

Table 2. Derived parameters of dust cores associated with H/UC HII regions: core identifier, integrated free-free flux at 1.3 mm estimated from the 3.3 cm map and from the H30 α line, percentage of free-free emission in Band 6, spectral index of free-free emission, and emission measure.

n	$F_{\text{ff,cm}}^{\text{int}}$ [mJy.b $^{-1}$]	$F_{\text{ff,RL}}^{\text{int}}$ [mJy.b $^{-1}$]	P_{ff} [%]	α	EM [pc cm $^{-6}$]
1	26.3	809.1	>78	>0.96	>2.9e8
2	27.6	422.5	>58	>0.74	>2.9e8
3	40.3	224.2	>61	>0.43	>2.9e8
4	-	90.4	96	-	-
5	-	71.5	54	-	-
7	29.2	115.3	>61	>0.32	>2.9e8
8	1.1	-	-	-	1.1e7
9	-	55.8	65	-	-
10	8.8	179.6	54	0.83	1.8e8
11	15.8	24.6	44	0.04	1.4e8
12	-	65.3	56	-	-
13	9.2	94.8	64	0.62	1.1e8
14	97.1	137.1	>67	>0.00	>2.9e8
15	43.2	39.5	67	-0.13	1.9e8
16	49.6	176.5	63	0.29	2.9e8
17	12.7	80.5	64	0.47	1.7e8
18	0.7	-	-	-	4.5e6
23	9.1	11.0	62	-0.04	8.3e7
29	12.4	17.6	75	0.01	9.5e7
39	-	17.9	59	-	-
40	39.4	40.5	51	-0.09	1.5e8
44	1.0	8.1	37	0.53	8.7e6
46	24.9	35.3	61	0.00	3.1e8
47	14.6	23.7	54	0.05	1.6e8
50	-	9.1	25	-	-
59	-	11.2	49	-	-
69	12.4	13.6	64	-0.07	4.2e7
72	22.4	19.1	45	-0.15	1.1e8
73	21.6	25.0	55	-0.06	1.7e8
74	2.6	2.9	33	-0.07	1.4e7
78	-	8.1	37	-	-
87	10.0	13.7	42	-0.01	1.3e7
94	-	13.8	54	-	-
104	0.5	-	-	-	9.1e6
107	-	7.1	48	-	-
112	-	16.7	65	-	-
116	2.4	3.6	73	0.02	9.9e6
117	1.7	-	-	-	1.3e7
131	-	1.3	40	-	-
147	-	4.4	22	-	-

We also constructed a pixel by pixel free-free map $I_{\text{ff,RL}}$ using the moment 0 of the H30 α recombination line (see, e.g., [Wilson et al. 2009](#); [Liu et al. 2019](#)):

$$I_{\text{ff,RL}} = 1.432 \times 10^{-4} (\nu_0^{-1.1} T_e^{1.15}) (1 + N_{\text{He}}/N_{\text{H}}) \int I_{\text{H30}} d\nu, \quad (2)$$

where the electron temperature is $T_e = 7000$ K (e.g. [Zhang et al. 2023](#)), the helium to hydrogen number ratio is $N_{\text{He}}/N_{\text{H}} = 0.08$, and ν_0 is the central frequency of the H30 α line. We then obtained a second evaluation of the free-free emission in B6 by measuring on the $I_{\text{ff,RL}}$ map the integrated fluxes of the cores, $F_{\text{ff,RL}}^{\text{int}}$, using the method presented in Section 3.1.

From the previous measurements, we derived various parameters for the cores associated with H/UC HII regions. We defined

their percentage of free-free emission in B6 as $P_{\text{ff}} = F_{\text{ff,RL}}/F_{\text{B6}}$. P_{ff} ranges from 22 to 96%. The dust flux in B6 is expressed as $F_{\text{B6,dust}} = F_{\text{B6}} - F_{\text{ff}}$, with $F_{\text{ff}} = F_{\text{ff,RL}}$ when the H30 α is detected, and $F_{\text{ff}} = F_{\text{ff,cm}}$ otherwise. By construction, $F_{\text{ff,RL}}$ can be expressed as a function of $F_{\text{B6,dust}}$ and P_{ff} : $F_{\text{ff,RL}} = F_{\text{B6,dust}} P_{\text{ff}} / (1 - P_{\text{ff}})$. We also computed the spectral index of free-free emission from ν_{BX} to ν_{B6} :

$$\alpha_{\text{ff}} = \frac{\log(F_{\text{ff,RL}}/F_{\text{BX}})}{\log(\nu_{\text{B6}}/\nu_{\text{BX}})} \quad (3)$$

Finally, we computed the emission measure, EM, of H/UC HII emission within dust cores:

$$\text{EM [pc cm}^{-6}] = \int n_e^2 dl = 12 \tau_{\text{ff}} \left[\frac{\nu_{\text{BX}}}{\text{GHz}} \right]^{2.1} \left[\frac{T_e}{\text{K}} \right]^{1.35}, \quad (4)$$

with n_e the electron density and τ_{ff} the free-free continuum optical depth, expressed as

$$\tau_{\text{ff}} = -\ln \left[\left(1 - \frac{T_{\text{B}}}{T_e} \right) \right], \quad (5)$$

The brightness temperature T_{B} is calculated from the maximum intensity in X band within the cores FWHM, $F_{\text{BX}}^{\text{max}}$, and we used a constant electron temperature $T_e = 7000$ K. Two cores with $T_{\text{B}} > 7000$ K (#3 and #16) and 4 cores with $6700 < T_{\text{B}} < 7000$ K (#1, #2, #7 and #14) are likely to have higher electron temperature, considering the condition $T_e > T_{\text{B}}$ set by Eq. (5). We computed for these six cores a lower limit of the emission measure using an opacity $\tau_{\text{ff}} = 1.5$ in line with the rest of the core sample. The emission measures of cores with H/UC HII regions range from 4.5×10^6 to 3.1×10^8 pc cm $^{-6}$, which are in the range of values found for ultra-compact HII regions ([Churchwell 2002](#); [Hoare et al. 2007](#)). Table 2 lists $F_{\text{ff,cm}}$, $F_{\text{ff,RL}}$, P_{ff} , α_{ff} , and EM for the 40 cores with robust and candidate H/UC HII emission.

4.3. Core classification

In what follows, we combine the statistics obtained from the detection rates of H/UC HII regions (see Section 4.1) with the hot molecular core (HMC) detections (see Section 3.3) to build a classification of the dust cores into four types: *a/* cores without either HMC or H/UC HII region, *b/* cores associated with a HMC but without H/UC HII emission, *c/* cores associated with both a HMC and H/UC HII emission, and *d/* cores associated with a H/UC HII region but without HMC emission. Within the full ALMA B6 mosaic, the number counts of each type are *a/*: 77 (81), *b/*: 12, *c/*: 7, and *d/*: 33 (29). Numbers in parenthesis correspond to the situation where all the cores with H/UC HII regions candidates are accounted in first type. Within the smaller field of view of the VLA X band map, the statistics are 69 (70), 12, 5 and 23 (22). Fig. 4 shows a diagram summarizing the detection statistics. In addition, 57 (58) H/UC HII regions without cores have been detected by Juárez-Gama et al. (in prep.).

5. Discussion

5.1. Evolution of Star Forming Cores in W49A

From the empirical classification presented in Section 4.3, in this section we propose an evolutionary sequence for the dust cores in W49A, based on the presence or absence of the analyzed indicators of high-mass star formation. Fig. 5 summarizes the proposed evolutionary scheme.

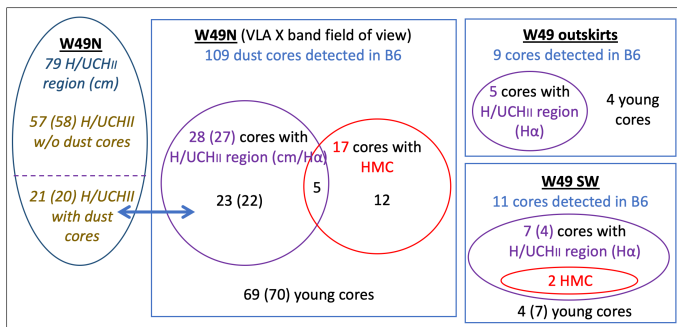


Fig. 4. Classification of the dust cores extracted in the ALMA Band 6 maps, based on the detection of HMCs and/or H α region emission. Cores lying within the field of view of the VLA map (W49N) are separated from cores in W49SW and in the eastern outskirts.

Cores in stage *a/* do not have evidence of a HMC or H/UC H α region, they are likely prestellar or low-mass protostellar cores. Among cores in stage *a/*, which we label "young cores", only a fraction are the precursors of high-mass stars. It is indeed expected that some of them will produce low-mass objects. From stage *b/* onward, all cores are expected to harbor a high-mass ($\gtrsim 8 M_{\odot}$) protostar. As it grows in mass, the protostellar object will first reach the luminosity necessary to heat its envelope to a temperature where complex organic molecules are released from dust grains. This defines the onset of the hot molecular core stage (*b/*, "young HMC" in Fig. 5). Later on, when the extreme ultraviolet (EUV) radiation of the star is sufficient to ionize atomic hydrogen, an H α region is born. During the short phase in which the HMC and the H/UC H α region coexist (stage *c/*, "evolved HMC"), we expect that the remaining dust and molecules form a cocoon around the H α region, which is mostly free of dust (Lizano 2008). The radiation then becomes strong enough to fully destroy molecules, and only some dust remains surrounding the H/UC H α region (stage *d/*, "intermediate UCH α "). Finally, the UCH α fully clears its way out of the now extinct core, which is not detected anymore in dust emission (stage *e/*, "evolved UCH α "). We expect that high-mass protostars keep accreting from their envelopes from stages *b/* to *d/*, which therefore represent the phases of high-mass protostellar evolution. Under this definition, 40 (39) cores out of 109 in W49N are high-mass protostellar cores. For W49SW and what we label as outskirts, 12 (9) cores out of 20 contain high-mass protostars (see Fig. 4).

Regarding their spatial distribution, the large majority of the cores detected at 1.3 mm (109 out of 129) lie within the central star forming region W49N. Only a few cores are located at distances beyond a parsec from the central hub (see Fig. 1). In W49N, HMCs and the well known H α regions (De Pree et al. 1997, 2018) co-exist with a population of young cores (see zoom-in Fig. 2). This indicates that the central protocluster is still actively forming stars in spite of the significant stellar feedback, as suggested by Galván-Madrid et al. (2013) from the measurement of a $\sim 2 \times 10^5 M_{\odot}$ molecular gas reservoir in W49N. A similar scenario has been proposed for the also very active W51-E and W51-IRS2 protoclusters (Ginsburg et al. 2016).

Using uncertainties from the binomial distribution, we measured the 75% confidence interval for the percentage of cores containing high-mass protostars (stages *b/* to *d/*) to be [30-42]% in W49N and [30-75]% in W49SW and the W49 outskirts. Therefore, the relative abundance of high-mass protostars does not appear to be statistically different between the center of W49A and its periphery. We reach the same conclusion when

only HMCs or cores with H/UC H α regions are considered. This suggests that the different sub-protoclusters analyzed in this paper have a similar "age", in the sense that their core and protostellar populations look statistically similar. The small number of objects in W49SW and the W49 outskirts forbids us to make a stronger statement, but this further suggests that star formation across the W49A cloud started simultaneously, possibly by cloud-cloud collision as suggested by Miyawaki et al. (2022a).

5.2. Ionization evolution within dust cores

The physical parameters derived in Section 4.2 allow us to evaluate the evolution of the protostar and envelope masses. The left panel of Fig. 6 shows that cores with a HMC and/or H/UC H α region have statistically higher dust flux than the others. The median dust flux of the two distributions are 2.2×10^{-2} Jy and 6.9×10^{-3} Jy, respectively. We have verified with a KS test that the distributions are statistically distinct (p -value of 4×10^{-7}). Since the dust flux is related to the molecular gas mass of the core, this difference suggests that the more evolved cores could also be more massive. Complementary, the right panel of Fig. 6 shows a strong correlation between the dust flux at 1.3 mm and the amount of free-free emission. Both the Pearson and Spearman correlation coefficients are higher than 0.8, with p -values $\approx 10^{-10}$. Since the amount of free-free emission is related to the mass of the central star through the number of ionizing photons (e.g., Kurtz et al. 1994), this correlation could indicate that the mass of the central (proto)star grows simultaneously with the mass of its gas envelope. This hypothesis is in line with models of continuous accretion across multiple scales (e.g., Smith et al. 2009; Vázquez-Semadeni et al. 2019), as well as with recent observations suggesting that cores grow in mass as they evolve from quiescent (candidate prestellar) to active protostellar stages (Nony et al. 2023).

However, the dust flux is also dependent on the dust temperature, which might be higher in the more evolved cores than in the younger ones. This could partially explain the difference between the distributions in the left panel of Fig. 6. For an envelope internally heated by an embedded protostar, the dust temperature depends on its luminosity (Scoville & Kwan 1976), hence on the protostellar mass. Therefore, the correlation found in the right panel of Fig. 6 between the dust and free-free fluxes could alternatively be explained by the dependence on the stellar mass of both quantities. Detailed measurements of core temperatures, which are beyond the scope of this work, are thus needed to draw firmer conclusions.

In Fig. 7 we compare the percentage of free-free emission in the 1.3 mm flux (P_{ff}) to the free-free spectral index (α_{ff}) between 3.3 cm and 1.3 mm, for the sample of dust cores with an estimation of their free-free content from both a centimeter continuum and H30 α detection (see Section 4.2). A first group of dust cores with optically thin free-free emission ($\alpha_{\text{ff}} \approx -0.1$ to 0) has P_{ff} spanning a large range of values, from 30 to 80%. In contrast, a second group of cores with partially optically thick free-free emission ($\alpha_{\text{ff}} \sim 0.3$ to 1) tends to show a more restricted $P_{\text{ff}} \approx 55 - 65\%$, with a couple of exceptions. To first order, H α regions are expected to smoothly evolve as they ionize and break out of their parental core (Keto 2007; Tanaka et al. 2016). During this process, they are expected to transition from denser objects with partially optically thick emission, to being less dense and optically thin (e.g., Keto et al. 2008; Galván-Madrid et al. 2009). HMCs represent an early stage within this sequence (see Section 5.1), therefore the fact that the three HMCs within the sample of dust cores with H α emission have partially optically

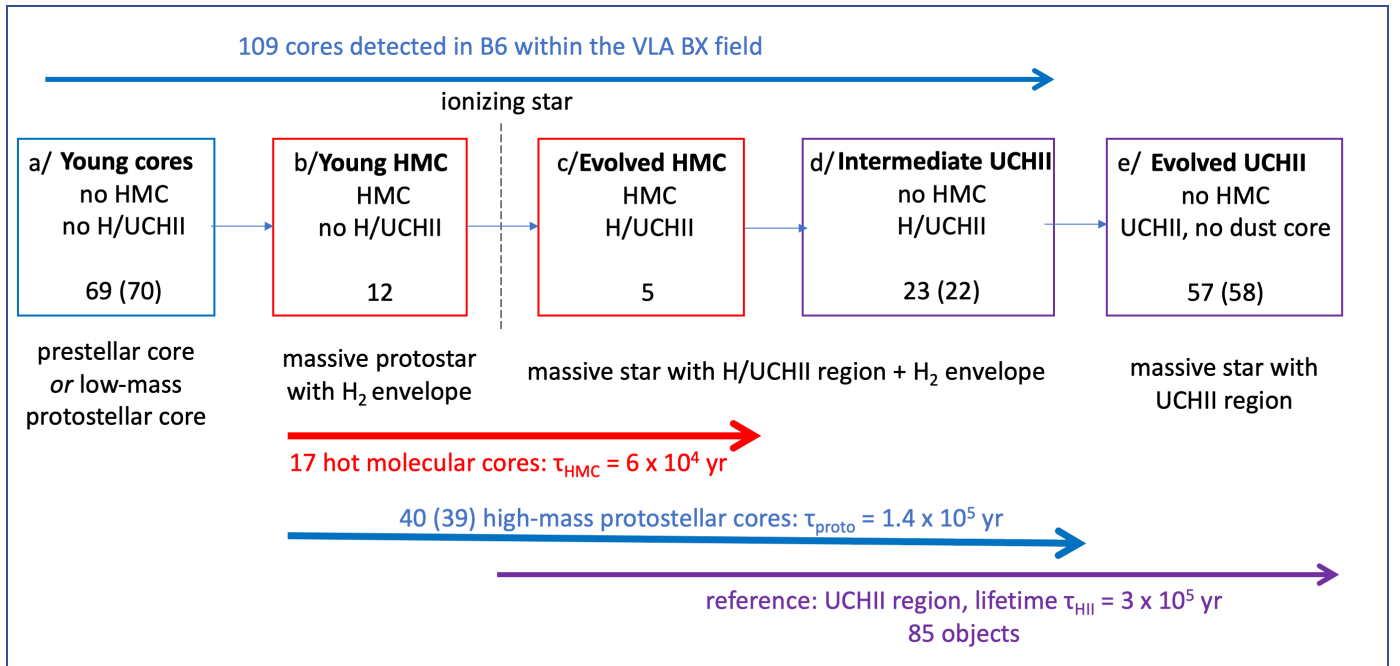


Fig. 5. Evolutionary sequence established for the cores extracted from the ALMA B6 maps within the X-band field of view (W49N), based on the presence or absence of hot molecular cores (HMC) and hyper/ultra-compact HII regions (H/UCHII). Statistical lifetimes for the various evolutionary stages are computed assuming a lifetime of the H/UC HII stage of $3 \times 10^5 \text{ yr}$ (see Section 5.3).

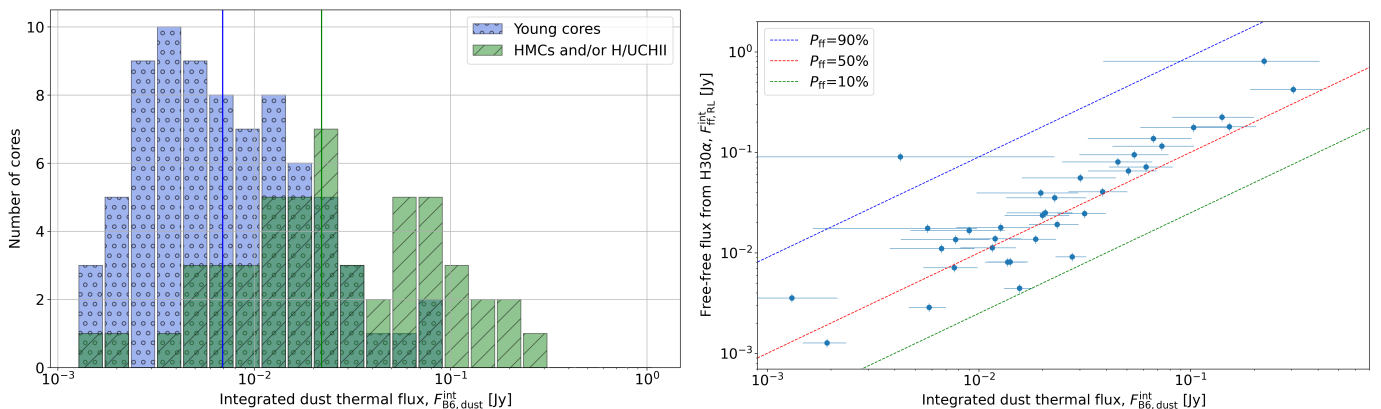


Fig. 6. Left: Distribution of the core-integrated dust fluxes. Cores with hot molecular core emission and/or H/UC HII region (stages b/ to d/, shown in green) are compared to the "young cores" without evidence of massive star formation (stage a/, shown in blue). Vertical lines represent the median value of the distributions. Right: Comparison between the free-free and dust fluxes. The core sample in this plot is made of the 35 cores with (robust or tentative) H30 α detection, classified as cores with H/UC HII region. Dashed lines represent constant values of the percentage of free-free emission P_{ff} with respect to the total core flux. Uncertainties are evaluated as 10% of the free-free and B6 fluxes.

thick free-free emission is consistent with this scenario. Under this simple interpretation, however, the points in Fig. 7 should follow an anti-correlation, or at least the – more evolved – optically thin HII regions should have on average a larger P_{ff} than the – younger – optically thicker ones. This is not observed. Previous work on hydrodynamical simulations with ionization feedback and synthetic observations has shown that the stochastic interactions of the neutral gas and ionizing photons can cause variations in the appearance of the youngest HII regions (Peters et al. 2010a), including their spectral indices (Peters et al. 2010b). This means that, even if H/UC HII regions eventually break free from their cores on timescales of $\sim 10^5 \text{ yr}$, their early evolution is not necessarily monotonic. We propose that this could be the cause of the observed spread of values in Fig. 7.

5.3. Lifetimes

We now proceed to evaluate the core lifetimes using the evolutionary sequence presented in Section 5.1 and shown in Fig. 5. For this purpose, we consider the population of 109 cores in W49N, for which the more complete search of H/UC HII regions has been made. Summing up 28 cores with H/UC HII regions and 57 H/UC HII regions not associated to a dust core, 85 objects fall in the H/UC HII regions category. Under the hypothesis of constant star-formation and assuming that HMCs are precursors of H/UC HII regions, the relative number of HMCs to H/UC HII regions (17/85) provides an estimation of their statistical lifetime. Using the typical lifetime for H/UC HII regions of $3 \times 10^5 \text{ yr}$, calculated from Galaxy-wide surveys (Churchwell 2002; Mottram et al. 2011), we estimate the lifetime of the HMC phase to be $\tau_{\text{HMC}} \approx (17/85) \cdot (3 \times 10^5) = 6 \times 10^4 \text{ yr}$. The ratio of 17 HMCs

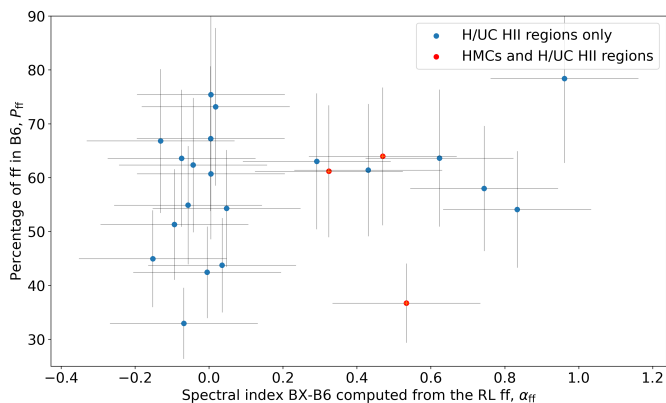


Fig. 7. The percentage of free-free emission P_{ff} at 1.3 mm (y-axis) is not anti-correlated with the spectral index of free-free emission (x-axis), from which two populations of cores can be distinguished. The core sample represented is 23 cores with H30 α and X band detections. Cores with H/UC H II regions and HMCs are shown in red, cores with H/UC H II regions only are shown in blue.

to 85 H/UC H II we find in W49, and thus the inferred lifetime, are smaller than previous estimations in the same region (6/12, Wilner et al. 2001) and in Sgr B2 (5/8, Bonfand et al. 2017). It is similar to that found in another high-mass star-forming region (1/9, Furuya et al. 2005). The period during which HMCs and H/UC H II regions coexist in W49A (5 cores out of 17) appears to be very short, $\approx 2 \times 10^4$ yr (see also the survey of Liu et al. 2021). Therefore, our results point toward a rapid dispersal of the warm, inner molecular envelope once the H II region appears.

We also use the relative number of high-mass protostellar cores to H/UC H II regions (40/85, see Section 5.1) to estimate the lifetime of the massive protostellar phase, $\tau_{\text{proto}} \approx 40/85 \times 3 \times 10^5 \approx 1.4 \times 10^5$ yr. Our estimation is about two times lower than the value reported in the review of Motte et al. (2018), $\tau_{\text{proto}} \sim 3 \times 10^5$ yr. It is also within the range of durations reported by Mottram et al. (2011), 7×10^4 yr to 4×10^5 yr for massive YSOs with luminosities from 10^4 to $10^5 L_{\odot}$. Our estimation of the lifetime of the massive protostellar phase may be a lower limit if we are missing detections of HMCs or H/UC H II regions. For example, it has been reported that a large dust optical depth could hinder the detection of molecular lines in emission (e.g. De Simone et al. 2020). Conversely, our estimation of the number of high-mass protostars may be an upper limit if some of the HMCs are associated with intermediate mass protostars which will not evolve to high-mass stars, or if our 3000 au-cores subfragment into several intermediate and low-mass stars.

6. Conclusions

We presented an analysis of the star-formation activity in W49 based on the first millimeter continuum survey in this region. Our main results and conclusions are as follows:

1. We built a 1.3 mm continuum image at $0.29'' \times 0.24''$ resolution from ALMA B6 observations and constructed a catalog of 129 cores, extracted using the *getsf* algorithm.
2. We looked for cores associated with H/UC H II regions by analyzing the VLA X band map (3.3 cm, De Pree et al. 2020), dominated by free-free emission, and the H30 α recombination line at 231.9 GHz, covered by our ALMA observations. We found a good agreement between these two tracers of ionized gas, with 23 common detections and only four cores

with H II regions detected only in the X band map, out of 109 cores within the VLA field of view.

3. We identified a total of 36 cores associated with H/UC H II regions over the entire ALMA mosaic, as well as four other cores tentatively associated with H/UC H II regions. We measured their integrated free-free flux and derived their dust flux at 1.3 mm.
4. The spectral indexes from 3.3 cm to 1.3 mm range from 1, for the youngest cores with partially optically thick free-free emission, to about -0.1, that is optically thin free-free emission obtained for cores allegedly more evolved. The emission measures, which range from 4.5×10^6 to 3.1×10^8 pc cm $^{-6}$, are typical of H/UC H II regions.
5. We also found, using the methyl formate doublet at 218.281 and 218.298 GHz within the spectral coverage of our ALMA B6 data, that 19 cores are associated with hot molecular core (HMC) emission. 17 HMCs are located within the central subregion, W49N, which is about three times the number of HMCs previously reported by Wilner et al. (2001). This places W49 among the protoclusters with the best statistics for HMCs studies, along with W43 and W51 (Brouillet et al. 2022; Bonfand et al. 2024).
6. We combined these two tracers of high-mass star formation (HMC and H II region emission) to propose a classification of the cores according to their evolutionary stage. Within W49N, covered by the VLA map, 69 cores without HMC or H/UC H II region are labeled as "young cores", meaning that they are either prestellar or lower-mass protostellar cores. The 5 cores with H/UC H II regions which are also associated with HMCs are assumed to be less evolved than the 23 cores with H/UC H II regions only. Finally we also considered a fifth category of H/UC H II regions not associated to dust cores.
7. The statistical lifetimes of the hot molecular core and massive protostellar phases in W49 are estimated to be 6×10^4 yr and 1.4×10^5 yr, respectively, based on a duration of the H/UC H II phase of 3×10^5 yr. The identification of massive protostellar cores is based on the association between a dust core and a HMC and/or an H/UC H II region. These estimations could be upper limits taking into the possible subfragmentation of HMCs into less massive protostars.
8. We found that HMCs and H/UC H II regions coexist in W49A during a short period of $\approx 2 \times 10^4$ yr. This indicates a rapid dispersal of the inner molecule envelope once the H/UC H II is formed.

Acknowledgements. We thank the referee R. Miyawaki for his helpful comments improving the manuscript. RGM and TN acknowledge support from UNAM-PAPIIT project IN108822 and from CONACyT Ciencia de Frontera project ID 86372. TN also acknowledges support from the postdoctoral fellowship program of the UNAM. Part of this work was performed using the high-performance computers at IRyA, Mexico, funded by CONACyT and UNAM. The work from the IT staff at this institute is acknowledged. AG acknowledges support from the NSF via grants AST 2008101 and CAREER 2142300. H.B.L. is supported by the National Science and Technology Council (NSTC) of Taiwan (Grant Nos. 111-2112-M-110-022-MY3). C R-Z acknowledges support from program UNAM-PAPIIT IG101723. This paper makes use of the following ALMA data: ADS/JAO.ALMA#2016.1.00620.S ALMA is a partnership of ESO (representing its member states), NSF (USA) and NINS (Japan), together with NRC (Canada), MOST and ASIAA (Taiwan), and KASI (Republic of Korea), in cooperation with the Republic of Chile. The Joint ALMA Observatory is operated by ESO, AUI/NRAO and NAOJ. This work is based on an analysis carried out with the GILDAS, IMAGER and CASSIS softwares, as well as the CDMS and JPL spectroscopic databases. CASSIS has been developed by IRAP-UPS/CNRS (<http://cassis.irap.omp.eu>).

References

- Barnes, A. T., Kauffmann, J., Bigiel, F., et al. 2020, *MNRAS*, 497, 1972
- Bonfand, M., Belloche, A., Menten, K. M., Garrod, R. T., & Müller, H. S. P. 2017, *A&A*, 604, A60
- Bonfand, M., Csengeri, T., Bontemps, S., et al. 2024, arXiv e-prints, arXiv:2402.15023
- Breen, S. L., Fuller, G. A., Caswell, J. L., et al. 2015, *MNRAS*, 450, 4109
- Brouillet, N., Despois, D., Molet, J., et al. 2022, *A&A*, 665, A140
- CASA Team, Bean, B., Bhatnagar, S., et al. 2022, *PASP*, 134, 114501
- Churchwell, E. 2002, *ARA&A*, 40, 27
- De Pree, C. G., Galván-Madrid, R., Goss, W. M., et al. 2018, *ApJ*, 863, L9
- De Pree, C. G., Mehringer, D. M., & Goss, W. M. 1997, *ApJ*, 482, 307
- De Pree, C. G., Wilner, D. J., Deblasio, J., Mercer, A. J., & Davis, L. E. 2005, *ApJ*, 624, L101
- De Pree, C. G., Wilner, D. J., Kristensen, L. E., et al. 2020, *AJ*, 160, 234
- De Simone, M., Ceccarelli, C., Codella, C., et al. 2020, *ApJ*, 896, L3
- Furuya, R. S., Cesaroni, R., Takahashi, S., et al. 2005, *ApJ*, 624, 827
- Galván-Madrid, R., Keto, E., Zhang, Q., et al. 2009, *ApJ*, 706, 1036
- Galván-Madrid, R., Liu, H. B., Zhang, Z. Y., et al. 2013, *ApJ*, 779, 121
- Ginsburg, A., Csengeri, T., Galván-Madrid, R., et al. 2022, *A&A*, 662, A9
- Ginsburg, A., Goss, W. M., Goddi, C., et al. 2016, *A&A*, 595, A27
- Gwinn, C. R., Moran, J. M., & Reid, M. J. 1992, *ApJ*, 393, 149
- Herbst, E. & van Dishoeck, E. F. 2009, *ARA&A*, 47, 427
- Hoare, M. G., Kurtz, S. E., Lizano, S., Keto, E., & Hofner, P. 2007, in *Protostars and Planets V*, ed. B. Reipurth, D. Jewitt, & K. Keil, 181
- Homeier, N. L. & Alves, J. 2005, *A&A*, 430, 481
- Keto, E. 2007, *ApJ*, 666, 976
- Keto, E., Zhang, Q., & Kurtz, S. 2008, *ApJ*, 672, 423
- Kurtz, S. 2005, in *Massive Star Birth: A Crossroads of Astrophysics*, ed. R. Cesaroni, M. Felli, E. Churchwell, & M. Walmsley, Vol. 227, 111–119
- Kurtz, S., Churchwell, E., & Wood, D. O. S. 1994, *ApJS*, 91, 659
- Lin, Y., Liu, H. B., Li, D., et al. 2016, *ApJ*, 828, 32
- Liu, H. B., Chen, H.-R. V., Román-Zúñiga, C. G., et al. 2019, *ApJ*, 871, 185
- Liu, H.-L., Liu, T., Evans, Neal J., I., et al. 2021, *MNRAS*, 505, 2801
- Lizano, S. 2008, in *Astronomical Society of the Pacific Conference Series*, Vol. 387, *Massive Star Formation: Observations Confront Theory*, ed. H. Beuther, H. Linz, & T. Henning, 232
- McGrath, E. J., Goss, W. M., & De Pree, C. G. 2004, *ApJS*, 155, 577
- Men'shchikov, A. 2021, *A&A*, 649, A89
- Miyawaki, R., Hayashi, M., & Hasegawa, T. 2009, *PASJ*, 61, 39
- Miyawaki, R., Hayashi, M., & Hasegawa, T. 2022a, *PASJ*, 74, 128
- Miyawaki, R., Hayashi, M., & Hasegawa, T. 2022b, *PASJ*, 74, 705
- Molet, J., Brouillet, N., Nony, T., et al. 2019, *A&A*, 626, A132
- Motte, F., Bontemps, S., & Louvet, F. 2018, *ARA&A*, 56, 41
- Mottram, J. C., Hoare, M. G., Davies, B., et al. 2011, *ApJ*, 730, L33
- Nony, T., Galván-Madrid, R., Motte, F., et al. 2023, *A&A*, 674, A75
- Peng, T. C., Wyrowski, F., van der Tak, F. F. S., Menten, K. M., & Walmsley, C. M. 2010, *A&A*, 520, A84
- Peters, T., Banerjee, R., Klessen, R. S., et al. 2010a, *ApJ*, 711, 1017
- Peters, T., Mac Low, M.-M., Banerjee, R., Klessen, R. S., & Dullemond, C. P. 2010b, *ApJ*, 719, 831
- Pouteau, Y., Motte, F., Nony, T., et al. 2022, *A&A*, 664, A26
- Rivera-Soto, R., Galván-Madrid, R., Ginsburg, A., & Kurtz, S. 2020, *ApJ*, 899, 94
- Rugel, M. R., Rahner, D., Beuther, H., et al. 2019, *A&A*, 622, A48
- Saral, G., Hora, J. L., Willis, S. E., et al. 2015, *ApJ*, 813, 25
- Scoville, N. Z. & Kwan, J. 1976, *ApJ*, 206, 718
- Sievers, A. W., Mezger, P. G., Bordeon, M. A., et al. 1991, *A&A*, 251, 231
- Smith, R. J., Longmore, S., & Bonnell, I. 2009, *MNRAS*, 400, 1775
- Tanaka, K. E. I., Tan, J. C., & Zhang, Y. 2016, *ApJ*, 818, 52
- Vázquez-Semadeni, E., Palau, A., Ballesteros-Paredes, J., Gómez, G. C., & Zamora-Avilés, M. 2019, *MNRAS*, 490, 3061
- Welch, W. J., Dreher, J. W., Jackson, J. M., Terebey, S., & Vogel, S. N. 1987, *Science*, 238, 1550
- Wilner, D. J., De Pree, C. G., Welch, W. J., & Goss, W. M. 2001, *ApJ*, 550, L81
- Wilson, T. L., Rohlfs, K., & Hüttemeister, S. 2009, *Tools of Radio Astronomy*
- Zhang, B., Reid, M. J., Menten, K. M., et al. 2013, *ApJ*, 775, 79
- Zhang, C., Zhu, F.-Y., Liu, T., et al. 2023, *MNRAS*, 520, 3245
- Zhang, Y., Tanaka, K. E. I., Tan, J. C., et al. 2022, *ApJ*, 936, 68

Appendix A: Core catalog

Table [A1](#) lists the physical properties, detection (or non detection) of H/UC H_{II} regions and hot molecular cores for the 129 cores detected at 1.3 mm in W49. The labels of H/UC H_{II} regions previously identified at the core positions are also given.

Table A1. Main characteristics of cores detected on the 1.3 mm continuum image.

n	R.A. Dec. [ICRS]	Region	Size ["×"']	PA	F_{B6}^{int} [mJy.beam ⁻¹]	$F_{\text{BX}}^{\text{int}}$ [mJy.beam ⁻¹]	HII	Cross ID	HMC
(1)	(2)	(3)	(4)	(5)	(6)	(7)	(8)	(9)	(10)
1	19:10:13.419 9:06:13.00	N	0.33×0.27	10	1031.9	36.6	BX+RL	G2a	
2	19:10:13.149 9:06:12.72	N	0.37×0.33	117	728.4	38.5	BX+RL	B2	
3	19:10:12.889 9:06:11.73	N	0.39×0.29	169	365.0	56.0	BX+RL	A2	
4	19:10:10.938 9:05:17.53	SW	0.31×0.27	166	94.6		RL	-	*
5	19:10:16.356 9:06:07.04	out	0.49×0.35	115	133.2		RL	O	
6	19:10:13.614 9:06:49.12	N	0.45×0.30	118	75.0	-			*
7	19:10:13.144 9:06:18.76	N	0.35×0.29	142	188.5	40.6	BX+RL	C	*
8	19:10:14.130 9:06:25.00	N	0.44×0.30	155	200.2	1.5	BX	J1	*
9	19:10:11.050 9:05:20.11	SW	0.44×0.40	17	85.9		RL	R	*
10	19:10:13.455 9:06:12.79	N	0.33×0.27	20	332.0	12.3	BX+RL	G2c	
11	19:10:15.369 9:06:14.95	N	0.40×0.33	174	56.2	22.0	BX+RL	N	
12	19:10:16.372 9:06:06.81	out	0.47×0.31	123	116.1		RL	O	
13	19:10:13.116 9:06:12.36	N	0.30×0.26	11	149.0	12.7	BX+RL	B1	
14	19:10:13.202 9:06:11.13	N	0.68×0.57	69	203.9	135.2	BX+RL	D	
15	19:10:13.340 9:06:21.37	N	0.56×0.47	97	59.1	60.1	BX+RL	F	
16	19:10:13.373 9:06:12.58	N	0.46×0.39	146	279.9	69.0	BX+RL	G1	
17	19:10:12.884 9:06:12.16	N	0.39×0.34	30	125.9	17.7	BX+RL	A1	*
18	19:10:13.312 9:06:19.87	N	0.44×0.32	172	93.3	1.0	BX	-	
19	19:10:14.645 9:06:25.97	N	0.41×0.40	143	20.3	-			*
20	19:10:13.279 9:06:12.79	N	0.39×0.29	0	82.6	-			*
22	19:10:14.628 9:06:45.96	N	0.38×0.33	6	10.5	-			
23	19:10:13.060 9:06:16.07	N	0.35×0.33	178	17.7	12.7	BX+RL	C1	
24	19:10:14.284 9:06:22.22	N	0.44×0.40	69	20.7	-			
25	19:10:15.358 9:06:15.36	N	0.36×0.33	167	21.3	-			*
26	19:10:12.665 9:06:07.57	N	0.48×0.44	71	25.0	-			
27	19:10:13.272 9:06:16.38	N	0.52×0.37	47	53.7	-			*
28	19:10:13.149 9:06:13.84	N	0.45×0.38	72	112.0	-			*
29	19:10:13.259 9:06:12.19	N	0.37×0.31	35	23.3	17.3	BX+RL	E3	
30	19:10:14.137 9:06:26.60	N	0.45×0.38	110	27.9	-			
31	19:10:14.312 9:06:22.21	N	0.37×0.27	23	11.7	-			
32	19:10:13.170 9:06:13.36	N	0.36×0.33	64	70.4	-			*
34	19:10:13.259 9:06:18.88	N	0.38×0.29	164	32.2	-			
35	19:10:13.441 9:06:07.11	N	0.28×0.25	27	4.5	-			
36	19:10:12.097 9:06:14.64	N	0.41×0.26	74	9.0	-			*
37	19:10:14.182 9:06:20.58	N	0.32×0.28	103	2.9	-			
39	19:10:11.671 9:05:26.86	SW	0.55×0.45	153	30.6		RL	S	
40	19:10:13.392 9:06:11.82	N	0.56×0.48	10	79.0	54.8	BX+RL	G1S	
42	19:10:14.664 9:06:25.53	N	0.45×0.36	107	12.0	-			
43	19:10:13.348 9:06:16.05	N	0.39×0.33	155	25.9	-			*
44	19:10:12.703 9:06:11.29	N	0.31×0.26	24	22.2	1.5	BX+RL	-	*
45	19:10:13.211 9:06:14.30	N	0.31×0.27	26	24.8	-			
46	19:10:13.498 9:06:11.77	N	0.36×0.32	179	58.1	34.7	BX+RL	G3b	
47	19:10:13.498 9:06:12.42	N	0.37×0.26	8	43.7	20.3	BX+RL	G3a	
48	19:10:13.721 9:06:44.58	N	0.37×0.33	53	3.6	-			
49	19:10:12.671 9:06:18.28	N	0.39×0.29	172	7.0	-			
50	19:10:10.686 9:05:16.78	SW	0.95×0.70	134	36.7		RL	R3	
51	19:10:12.644 9:06:18.93	N	0.39×0.30	37	4.0	-			
52	19:10:16.504 9:06:04.24	out	0.63×0.53	23	11.4				
53	19:10:13.364 9:06:18.01	N	0.44×0.41	88	10.3	-			
54	19:10:13.323 9:06:16.32	N	0.33×0.30	27	16.8	-			*
55	19:10:13.230 9:06:54.16	N	0.72×0.58	130	4.1	-			
56	19:10:13.188 9:06:12.85	N	0.45×0.36	0	81.5	-			*
57	19:10:13.114 9:06:13.77	N	0.42×0.37	120	62.3	-			
58	19:10:16.666 9:05:49.88	out	0.44×0.32	53	7.2				
59	19:10:16.402 9:06:07.36	out	0.47×0.36	143	22.8		RL	-	
60	19:10:15.754 9:06:05.78	N	0.49×0.40	169	4.7	-			

(1) Core number in the getsf catalog. (2) Right Ascension and Declination coordinates. (3) Subregion: (W49-)N, (W49-)SW or (W49-)out(skirts). (4) FWHM major and minor axis. (5) Position Angle (West to North) of the ellipse. (6,7) Integrated fluxes in B6 and BX. (8) Detection of the H/UC HII region in X band 3.3 cm (BX) and/or in H30 α (RL). (9) Identification of the associated H/UC HII region in the catalogs of [De Pree et al. \(1997, 2020\)](#). (10) Cores associated to hot molecular core emission are marked with *.

Table A1 – continued from previous page

n	R.A. Dec.		Region	Size	PA	F_{B6}^{int}	$F_{\text{BX}}^{\text{int}}$	HII	Cross ID	HMC
(1)	[ICRS]		(3)	["×"]	(5)	[mJy.beam ⁻¹]	[mJy.beam ⁻¹]	(8)	(9)	(10)
61	19:10:15.256	9:06:10.99	N	0.32×0.29	92	2.1	-			
62	19:10:12.843	9:06:11.44	N	0.61×0.42	149	76.7	-			
63	19:10:14.605	9:06:26.38	N	0.45×0.32	4	7.2	-			
65	19:10:14.159	9:06:21.56	N	0.60×0.54	110	14.2	-			
66	19:10:13.385	9:06:19.37	N	0.40×0.36	37	19.7	-			
67	19:10:13.656	9:06:21.49	N	0.57×0.43	46	10.0	-			
68	19:10:12.800	9:06:27.54	N	0.54×0.34	85	6.9	-			
69	19:10:14.186	9:06:15.32	N	0.66×0.41	42	21.3	17.2	BX+RL	J	
70	19:10:12.746	9:06:10.33	N	0.36×0.32	53	24.0	-			
71	19:10:13.434	9:06:22.78	N	0.46×0.36	155	7.1	-			
72	19:10:13.178	9:06:18.28	N	0.50×0.40	143	42.5	31.2	BX+RL	C	
73	19:10:13.601	9:06:11.02	N	0.43×0.30	0	45.6	30.1	BX+RL	G3d	
74	19:10:14.563	9:06:20.47	N	0.50×0.40	50	8.7	3.6	BX+RL	L	
75	19:10:14.126	9:06:24.28	N	0.33×0.21	20	17.8	-			
76	19:10:13.323	9:06:25.53	N	0.47×0.31	124	6.0	-			
77	19:10:13.898	9:06:36.91	N	0.29×0.24	47	1.5	-			
78	19:10:16.344	9:06:07.75	out	0.53×0.49	111	21.8	-	RL	-	
79	19:10:13.018	9:06:17.05	N	0.60×0.55	90	16.2	-			
80	19:10:10.801	9:05:19.45	SW	1.03×0.77	137	25.9	-			
81	19:10:14.610	9:06:02.65	N	0.47×0.37	41	6.0	-			
82	19:10:14.178	9:06:26.65	N	0.34×0.29	55	9.1	-			
83	19:10:13.135	9:06:13.45	N	0.43×0.38	75	83.7	-			
84	19:10:12.329	9:06:18.58	N	0.28×0.25	176	2.0	-			
85	19:10:12.720	9:06:28.69	N	0.30×0.28	18	2.8	-			
86	19:10:13.234	9:06:12.68	N	0.44×0.40	177	49.8	-			
87	19:10:14.184	9:06:14.37	N	1.05×0.94	178	32.2	13.9	BX+RL	J	
88	19:10:12.613	9:06:22.60	N	0.43×0.31	168	3.5	-			
89	19:10:13.231	9:06:08.87	N	0.53×0.38	152	9.6	-			
90	19:10:15.433	9:06:16.78	N	0.43×0.32	11	3.3	-			
91	19:10:11.174	9:05:53.85	N	0.45×0.34	12	3.1	-			
92	19:10:12.685	9:06:32.36	N	0.97×0.90	127	7.3	-			
93	19:10:15.317	9:06:14.80	N	0.54×0.34	5	13.4	-			
94	19:10:14.509	9:06:22.47	N	1.06×0.82	67	25.7	-	RL	L	
95	19:10:11.487	9:05:32.14	N	0.31×0.27	24	2.4	-			
96	19:10:13.571	9:06:21.34	N	0.47×0.35	173	9.9	-			
97	19:10:13.307	9:06:17.02	N	0.37×0.29	162	15.2	-			
98	19:10:14.796	9:06:44.25	N	0.68×0.47	81	5.8	-			
99	19:10:15.807	9:06:05.59	N	0.29×0.27	157	1.4	-			
100	19:10:11.490	9:06:24.34	N	0.35×0.29	11	1.5	-			
101	19:10:13.459	9:06:20.14	N	0.49×0.32	144	15.4	-			
102	19:10:12.779	9:06:11.13	N	0.34×0.29	24	19.5	-			
103	19:10:14.825	9:06:36.88	N	0.69×0.50	140	5.1	-			
104	19:10:14.037	9:06:23.56	N	0.41×0.35	122	15.5	0.7	BX	-	*
105	19:10:13.630	9:06:20.30	N	1.03×0.86	146	33.5	-			
106	19:10:12.720	9:06:28.38	N	0.41×0.39	52	4.5	-			
107	19:10:16.297	9:06:06.66	out	0.55×0.40	157	14.8	-	RL	-	
108	19:10:13.719	9:06:25.03	N	0.40×0.34	111	5.1	-			
109	19:10:14.237	9:06:28.51	N	0.48×0.37	162	11.0	-			
110	19:10:15.409	9:06:11.87	N	0.65×0.36	2	5.8	-			
111	19:10:11.629	9:06:16.03	N	0.35×0.26	172	3.4	-			
112	19:10:11.731	9:05:27.37	SW	0.67×0.43	10	25.7	-	RL	S	
113	19:10:10.277	9:05:14.07	SW	0.30×0.23	160	4.5	-			
114	19:10:12.838	9:06:29.46	N	0.34×0.27	180	3.0	-			
115	19:10:16.826	9:05:49.99	out	0.83×0.66	4	11.1	-			
116	19:10:14.747	9:06:25.65	N	0.50×0.34	150	4.9	3.4	BX+RL	M	
117	19:10:13.683	9:06:10.06	N	0.36×0.34	119	6.4	2.4	BX	-	
119	19:10:10.956	9:05:18.60	SW	0.34×0.25	90	2.5	-			

(1) Core number in the getsf catalog. (2) Right Ascension and Declination coordinates. (3) Subregion: (W49-)N, (W49-)SW or (W49-)out(skirts). (4) FWHM major and minor axis. (5) Position Angle (West to North) of the ellipse. (6,7) Integrated fluxes in B6 and BX. (8) Detection of the H/UC HII region in X band 3.3 cm (BX) and/or in H30 α (RL). (9) Identification of the associated H/UC HII region in the catalogs of [De Pree et al. \(1997, 2020\)](#). (10) Cores associated to hot molecular core emission are marked with *.

Table A1 – continued from previous page

n	R.A. Dec.		Region	Size	PA	F_{B6}^{int}	$F_{B\lambda}^{\text{int}}$	HII	Cross ID	HMC
(1)	[ICRS]		(3)	["×"]	(5)	[mJy.beam ⁻¹]	[mJy.beam ⁻¹]	(8)	(9)	(10)
120	19:10:14.284	9:06:32.28	N	0.55 × 0.53	52	11.3	-			
121	19:10:14.253	9:06:29.98	N	0.42 × 0.35	115	4.0	-			
122	19:10:12.416	9:06:06.76	N	0.75 × 0.64	72	8.4	-			
123	19:10:10.758	9:05:21.46	SW	0.30 × 0.23	34	1.7	-			
124	19:10:13.735	9:06:49.42	N	0.44 × 0.40	147	4.4	-			
125	19:10:14.685	9:06:45.97	N	0.33 × 0.24	12	2.4	-			
126	19:10:13.779	9:06:16.81	N	0.38 × 0.26	15	3.5	-			
128	19:10:16.708	9:05:49.17	out	0.34 × 0.27	73	3.4	-			
130	19:10:13.780	9:06:22.11	N	0.37 × 0.29	173	4.1	-			
131	19:10:10.541	9:05:14.08	SW	0.30 × 0.25	124	3.2	-	RL	Q	
133	19:10:14.122	9:06:26.01	N	0.39 × 0.35	65	9.9	-			*
138	19:10:14.525	9:06:28.78	N	0.40 × 0.30	173	1.7	-			
140	19:10:14.262	9:06:26.22	N	0.36 × 0.26	117	3.0	-			
141	19:10:13.980	9:06:24.90	N	0.34 × 0.27	103	2.9	-			
142	19:10:14.980	9:06:03.82	N	0.30 × 0.23	142	1.7	-			
147	19:10:10.893	9:05:16.78	SW	0.95 × 0.68	152	20.0	-	RL	-	